Applied Catalysis B: Environmental 95 (2010) 335–347

Contents lists available at ScienceDirect

Applied Catalysis B: Environmental

journal homepage: www.elsevier.com/locate/apcatb

Flame-assisted synthesis of nanoscale, amorphous and crystalline, spherical $BiVO_4$ with visible-light photocatalytic activity

Nikola C. Castillo [a,b], Andre Heel [a,*], Thomas Graule [a], Cesar Pulgarin [b,**]

[a] Laboratory for High Performance Ceramics, EMPA - Swiss Federal Laboratories for Materials Testing and Research, Überlandstrasse 129, 8600 Dübendorf, Switzerland
[b] École polytechnique fédérale de Lausanne (EPFL), Faculté des Sciences de Base, Institut des Sciences et Ingénierie Chimiques, Groupe de Génie Électrochimique, CH-1015 Lausanne, Switzerland

ARTICLE INFO

Article history:
Received 31 August 2009
Received in revised form 12 January 2010
Accepted 18 January 2010
Available online 25 January 2010

Keywords:
Nanocrystalline materials
Bismuth vanadate
Visible light photocatalysis
Methylene blue
N-demethylation

ABSTRACT

The synthesis of bismuth vanadate ($BiVO_4$) nanoparticles has drawn considerable attention to their application as a visible-light-driven photocatalyst. Several techniques are addressing the enlargement of surface area, but some of them can cause impurities and lower the performance of the material. In this work, flame spray synthesis technique was used as a simple, easy upscalable technique to produce $BiVO_4$ powders. The effect of process parameters on particle properties such as size, morphology and crystallinity were investigated by several techniques: BET, XRD, DSC, TEM, DRS and ζ potential. Spherical $BiVO_4$ nanoparticles with either amorphous or monoclinic phase-pure crystal structure, along with specific surface areas (SSA) between 10 and 75 $m^2\,g^{-1}$ were obtained by a setup including an *in situ* crystallization step at $T \geq 270\,^{\circ}C$ on the powder collection site, sometimes followed by a mild or severe annealing post-treatment. Traditional synthesis routes usually require such annealing post-treatment which implies considerable loss of SSA. The photocatalytic activity of the as-prepared powders was investigated by the degradation of the cationic dye methylene blue (MB). *N*-demethylation of the dye was clearly identified as one of the degradation pathways, while ring cleavage was only observed with crystalline samples. Crystallinity and SSA were crucial parameters for the photocatalytic activity of different samples of $BiVO_4$ depending on the pH of the solutions. The control of these two parameters during the synthesis of $BiVO_4$ qualifies this method for a potential large scale production.

© 2010 Elsevier B.V. All rights reserved.

1. Introduction

Heterogeneous photocatalytic reactions (photocatalysis) [1] for the degradation of organic pollutants are an alternative to traditional wastewater treatment methods that often lead to hazardous byproducts [2]. Irradiation of an aqueous suspension of TiO_2 nanoparticles in presence of dissolved O_2 leads to the generation of so-called reactive oxygen species (ROS) such as OH radical and O_2^- anion. In this process, crystalline nanoparticles are required to prevent charge recombination after the absorption of light. The lifetime of a photo-excited electron in a semiconductor depends on the crystallinity of the particle and on the probability to react with an acceptor on the surface of the particle. Therefore, nanoscaled particles enhance the number of electrons that are likely to undergo electron transfer because the path between their formation site and the surface is much shorter. In the case of TiO_2, UV light is required due to its large bandgap (3.2 eV for anatase). Because UV light represents only a few percent of the energy of solar light, efforts are directed towards a more effective harvesting of solar energy, i.e. the development of visible light-active photocatalysts. There are two strategies to achieve this: (i) modification of TiO_2 properties by cationic or anionic doping [3]; and (ii) exploration of new kinds of semiconductors whose band edge positions approach the ideal photocatalyst. The first option implies structure defects that are inherent to the introduction of impurities and often leads to an increased recombination rate despite the gain in light absorption. TiO_2 has been recognized as the best monometallic oxide but recent works have explored the combination of oxides containing more than one metal element [4]. This offered many more combination possibilities and opened the field of "band engineering" [5].

$BiVO_4$ was first suggested as a photocatalyst by Kudo et al. for a photo-electrochemical water splitting application [6]. It has also been used for the degradation of pollutants such as organic dyes [7–10] and phenolic compounds [11–13]. A number of preparation techniques have been investigated by Kudo and coworkers during the past decade for photocatalytic applications: solid state [14]; aqueous processes including a calcination step [6] – either under

* Corresponding author.
** Corresponding author. Tel.: +41 21 693 47 20; fax: +41 21 693 47 22.
E-mail addresses: andre.heel@empa.ch (A. Heel), cesar.pulgarin@epfl.ch (C. Pulgarin).

0926-3373/$ – see front matter © 2010 Elsevier B.V. All rights reserved.
doi:10.1016/j.apcatb.2010.01.012

Table 1
Typical specific surface areas (S_{BET}) of crystalline $BiVO_4$ powders synthesized by different methods.

Synthesis	S_{BET} ($m^2 g^{-1}$)	Precursors	Comment	References
Alfa Aesar	0.45	N/A	Commercial powder.	[22]
Solid state	1.8	BN, [a] AV [b]	Calcination at 973 K for 8 h.	[10]
Metalorganic decomposition	N/A	$Bi(hex)_3$, [c] $VO(acac)_2$ [d] in acetylacetone	Pyrolysis of concentrated solutions at 400–500 °C for 2–15 h. μm domain size.	[23]
RT aqueous process	2.4	Layered alkali vanadates, $Bi(NO_3)_3$ in H_2O	Stirring of precursors in H_2O at RT for 3 days. Phase control over reaction time.	[6]
Hydrolysis at RT	N/A	BN, Na_3VO_4	Reaction time up to 46 h. μm domain size.	[16]
Homogeneous precipitation	0.2	BN, AV in aqueous HNO_3	Hydrolytic precipitation at 363 K for 8h.	[11]
Hydrothermal	0.3–2.6	BN, AV	Nanorods. Precipitation of solutions with different pH at 453 K for 48 h.	[15]
Sol–gel-like hydrothermal	13	BN, AV, CTAB in aqueous HNO_3	Nanofibers. Use of cationic surfactant to increase SSA. Precipitation at 160 °C for 48 h.	[17]
Ammonia coprecipitation	7.8–26	BN, AV in aqueous HNO_3	Solution basified by NH_3 addition. Includes calcination step at 473–773 K for 5 h.	[10]
Aqueous precipitation at RT	N/A	BN in aqueous organic base, AV in aqueous HNO_3	RT precipitation for 11 days. μm domain size.	[24]
Ultrasonic spray pyrolysis	3.2	BN, AV in aqueous HNO_3	Rapid calcination in tubular furnace at 700 °C.	[22]
Flame spray pyrolysis	17	$Bi(hex)_3$, VO naph. [e] in toluene-EH [f]	*in situ* crystallization at $T \geq 342$ °C.	[25]
Flame-assisted synthesis	14–35	BN, $VO(acac)_2$ in EtOH–HNO_3	High S_{BET} and high production output.	This work

[a] $Bi(NO_3)_3 \cdot 5H_2O$.
[b] NH_4VO_3.
[c] Bismuth (III) 2-ethylhexanoate.
[d] Vanadium (IV) (oxy)acetylacetonate.
[e] Vanadyl naphthenate.
[f] 2-Ethylhexanoic acid.

hard conditions like in hydrothermal synthesis [15] or simple room temperature conditions [16]; but also by a sol–gel-like route [17]. Other methods include hydrolysis of alkoxides [18], sonochemical precipitation of an aqueous solution [8] and metalorganic decomposition [19]. However, some of these methods last several hours or even days. Moreover, most of them yield powders with rather low surface areas (SSA ≤ 1 $m^2 g^{-1}$, see Table 1). High surface area – and here in particular the small particle diameter – is generally a benefit in heterogeneous catalysis. This is especially important in semiconductor photocatalysis when the oxidation of the pollutant occurs through direct hole oxidation after an adsorption step [20]. The synthesis of different morphologies might help to increase the available surface area but also to decrease the diffusion length between the site of photon absorption and the surface of the photocatalyst. Fibers, sheets and other 3D-frameworks have been reported [21]. Several techniques are currently addressing the enhancement of surface area using synthesis routes that involve inorganic additives, which can cause impurities and lower the performance. It may also complicate the synthesis and increase the costs in case of an industrial application.

Flame processes allow the synthesis of a wide range of homogeneous and nanoscaled oxides with varying compositions and crystalline phases, due to high temperatures and high quenching rates. A number of heterogeneous catalysts have been produced by this method [26], but also amorphous powders like fumed silica [27]. The synthesis of photocatalysts by flame processes has been reported by this group [28,29] and yielded high surface area, non-porous spherical nanoparticles. Degussa P25 TiO_2, the reference material in this field, is also prepared by a flame process [30]. In this article, the synthesis of high-surface area amorphous and monoclinic spherical nanoparticles of $BiVO_4$ towards their photocatalytic application is addressed. The goal and challenge being to obtain a high-surface area – yet crystalline – $BiVO_4$, based on the theoretical requirements defined for an ideal photocatalyst. The activity for the degradation of methylene blue (MB) is evaluated with respect to surface area, crystallinity and temperature history of the synthesis. The interaction of the photocatalyst and the dye is also investigated as a function of pH.

2. Experimental

2.1. Precursor solution for flame spray synthesis

The liquid precursor solution was prepared by the addition of $Bi(NO_3)_3 \cdot 5H_2O$ 98.5% (Riedel-de-Haën, Germany) into EtOH 99.9% followed by the addition of HNO_3 65%, puriss. p.a. (Fluka, Switzerland). The suspension was sonicated for 15 min until the white crystals were completely dissolved. Subsequently a stoichiometric amount of turquoise powder of $VO(acac)_2$ 99% (ACROS Organics, USA) was added under magnetic stirring and heating at 50 °C to yield a homogeneous green solution with an equimolar concentration of $c(Bi) = c(V) = 0.15$ M and an overall cation concentration of 0.30 M.

2.2. Powder synthesis by FSS

The experimental apparatus is shown in Fig. 1. The flame spray device consists of mass flow controllers for gases and syringe pumps for liquids, a spray burner and a powder collection unit. The burner is a block nozzle of a commercial flame cutter (Type 150–200, Pangas, Switzerland) with a 3 mm outlet diameter and six supporting flames (outlet diameter 1 mm) surrounding the center gas outlet at a distance of 1.5 mm. A capillary tube (1.6 mm outer diameter, 1.05 mm inner diameter) was placed concentrically in the center gas outlet for atomizing the liquid precursor to form an external mixing nozzle. The flow rate of the precursor was controlled volumetrically via a double syringe pump between 1 and 30 mL min^{-1} (PN1610, Postnova, Germany) to the capillary tube. Droplet aerosol was created by atomizing the liquid precursor at the exit of the capillary by oxygen (99.95%, Carbagas, Switzerland) supplied through the center gas outlet. Oxygen (99.95%, Carbagas, Switzerland) and acetylene (99.6%, Carbagas, Switzerland) for the supporting flames were pre-mixed in the block nozzle with an overall flow rate of 30 L min^{-1}, which was kept constant for all series of experiments. The flow rate of acetylene was varied between 9 and 13 L min^{-1}, and that of oxygen accordingly in order to change the exhaust gas temperature by changing the energy density. All gas flow rates were metered by

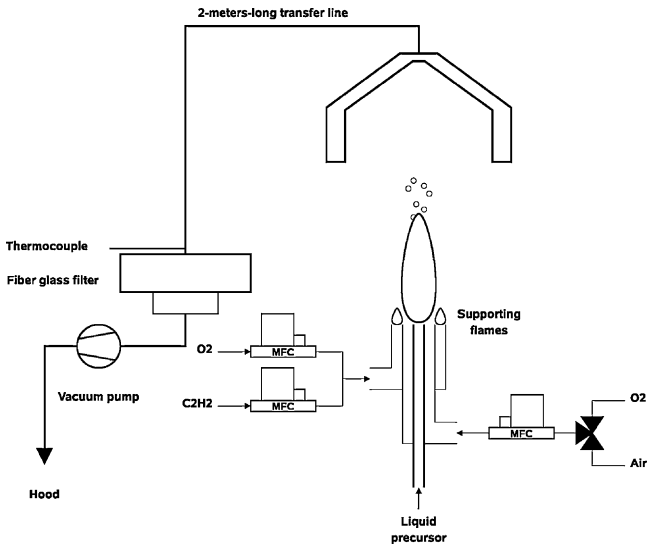

Fig. 1. Schematic diagram of the experimental setup for $BiVO_4$ nanoparticle synthesis.

mass flow controllers (MFC, Bronkhorst, the Netherlands). The powder produced was collected as a filter cake on a glass fiber filter (GF/A 150 mm, Whatman, UK) by means of a vacuum pump (VCA 25, Rietschle-Thomas, Switzerland).

Dispersion oxygen is both the driving force for the atomization of the liquid into the flame and a source of oxygen for the combustion of the precursor solution. Because this setup implies a turbulent flame, atmospheric air is also involved in the combustion reaction. The characteristics of the powders were found not to depend only on the process parameters $\dot{V}_{pr}$ and $\dot{V}_{O_2}$, but rather on the collection temperature of the powder on the filter T_{coll}. T_{coll} does in turn depend on the heat flow $\dot{Q}$ reaching the filter. $\dot{Q}$ can be controlled by the dilution of the aerosol in the flame. T_{coll} was purposedly lowered by increasing the dilution of the gas in the flame. Cool air surrounding the flame was sucked to varying extents into the transfer line leading to the filters. Thus less crystalline, and eventually amorphous powders could be selectively obtained.

As a reference, an additional annealing post-treatment of some flame-made powders was performed in a furnace (Heraeus instruments Thermicon P) under environmental air with a heating ramp of 10 °C min^{-1}.

2.3. Particle characterization

X-ray powder diffraction (XRD) was used for identification of the crystal phases. Diffraction measurements were performed with a PANalytical X'Pert PRO MPD instrument using Ni-filtered Cu Kα radiation. A 2θ scan range from 10 to 80°, a scanning step size of 0.0167° and a scintillation counter detector were used. Samples were measured in a reflection configuration (Bragg–Brentano geometry).

The specific surface area (SSA) of the product powder was determined from a 5-point N_2 adsorption isotherm obtained from the BET method on a Beckman-Coulter SA3100. Prior to BET analysis, the powder samples were degassed at 180 °C for 180 min under flowing N_2 atmosphere to remove adsorbed H_2O from the surface. Assuming dense, monodisperse and spherical particles, the BET-equivalent particle diameter (d_{BET}) was estimated by Eq. (1):

$$d_{BET} = \frac{6}{\rho \times SSA} \quad (1)$$

where ρ is the particle density, $\rho = 6.96$ kg dm^{-3}, as calculated by the program Jana2006 [31].

Differential scanning calorimetry (DSC) and thermogravimetric analysis (TGA) were performed in alumina crucibles on a NETZSCH STA 409 C/CD instrument under synthetic air with a heating rate of 10 K min^{-1}. The primary particle size, shape and morphology of the particles were investigated by transmission electron microscopy (TEM). Powder samples were dispersed ultrasonically in MilliQ water and a few drops of the dispersion were dried directly on carbon-coated copper grids (Plano GmbH, Germany). The TEM analysis was performed by a Philips CM30 electron microscope operating at 300 kV. Free software ImageJ (along with the Cell Counter plug-in) was used for particle counting on TEM images. Diffuse Reflectance UV–VIS spectroscopy (DRS) was applied to measure absorption of $BiVO_4$ with a Varian Cary 1E UV–Visible spectrophotometer equipped with a home-made spherical mirror device to concentrate diffuse reflection. A Kodak analytical $BaSO_4$ standard white reflectance coating was used as reference. The Kubelka–Munk relation Eq. (2) was used to transform reflectance data into the Kubelka–Munk function $\mathcal{F}(R_\infty)$, which is proportional to absorption:

$$\frac{K}{S} = \frac{(1 - R_\infty)^2}{2R_\infty} \equiv \mathcal{F}(R_\infty) \quad (2)$$

where K/S is the absorption over scattering ratio (scattering is assumed to be constant for $\lambda > 250$ nm) and R_∞ is diffuse reflectance [32]. ζ-potential measurements were made on a Malvern Zetasizer Nano-ZS with folded capillary measurement cells. Powders were dispersed in MilliQ water, at concentrations of 220 mg L^{-1} at 25 °C. The pH was swept from 5.1 to 2.0 by addition of diluted HCl.

2.4. Photocatalysis

Photocatalytic activity was evaluated in cylindrical Pyrex glass reactors with a top septum lid for sampling. A 50 mL aqueous solution was aerated under magnetic stirring (500 rpm) and exposed to the irradiation of five 18 W Philips TLD fluorescent tubes (emission maximum at $\lambda = 445$ nm [33], i.e. in a region where the absorbance of MB is negligible (Fig. 2). The global radiation flux at reactors distance was determined as 58 W m^{-2}). Two ventilation fans ensured a stable temperature of 25 °C inside the reactors throughout the experiments (Fig. 3). 5.0 mg of photocatalyst powder were dispersed ultrasonically in 49.0 mL of MilliQ water after what 1.0 mL of a methylene blue (pure USP,

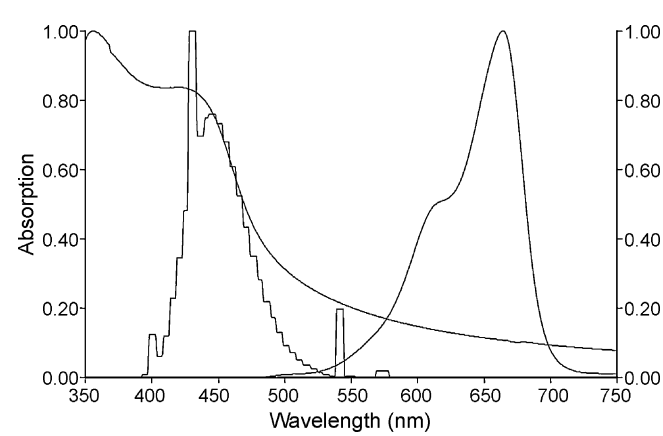

Fig. 2. UV–vis absorption spectrum of a MB aqueous solution (λ_{max} 664 nm), a crystalline $BiVO_4$ colloidal suspension (threshold at *ca.* 500 nm) and the emitted light intensity spectrum of the blue TLD fluorescent tubes (λ_{max} 445 nm) [33]. All intensities normalized for visibility.

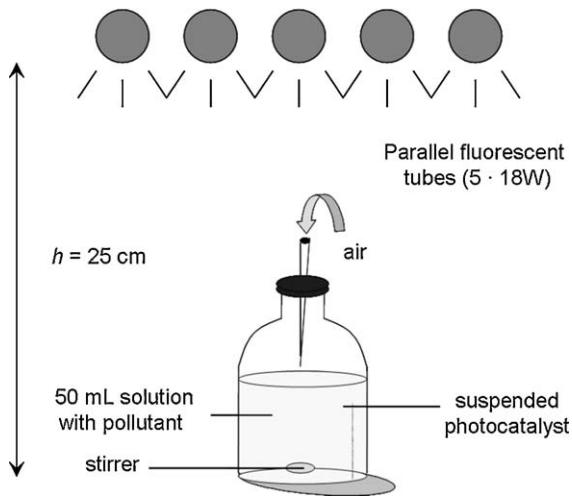

Fig. 3. Setup of the photocatalytic system.

AppliChem GmbH, Germany) solution was added to the reactor. Concentration of the photocatalyst was therefore 0.1 g L^{-1} in all runs and $c_0(MB) = 10^{-5}$ M (3.2 ppm), either at natural pH ($\simeq$5.5) or 8.5 by NaOH addition.

Nine 1.0 mL aliquots were collected at pre-established reaction times with a syringe and subsequently centrifuged (5 min at 5000 rpm) prior to UV–vis analysis. Decolorization was followed by UV–vis absorbance in acryl cuvettes between 350 and 750 nm in a Varian Cary 1E UV–Visible spectrophotometer. Dark adsorption was also measured over 5 h with equilibrium largely reached after 15 min.

Total organic carbon (TOC) was measured by a Shimadzu TOC-VSCN analyzer.

3. Results and discussion

3.1. Powder synthesis and characterization

As a preliminary work, process parameters of the flame spray synthesis (FSS) and their output were investigated keeping in mind the issue of crystalline *vs.* amorphous powders. For this reason XRD analyses were immediately carried out on all powders. The powders were classified either as *crystalline* or *amorphous* based on the presence or absence of diffraction peaks. Crystalline samples are vivid yellow while amorphous ones are orange yellow. All powders were labeled $BiVT_{coll}$, where T_{coll} is the collection temperature of the sample in °C (Table 2).

3.1.1. Role of temperature on the collection filter and in the flame

The synthesis of $BiVO_4$ by a flame process was very recently reported for pigmentary applications. In their paper, Strobel et al. pointed out that one way to obtain crystalline, monoclinic bismuth vanadate (mBiVO$_4$) is to allow an *in situ* crystallization on the powder collection filter [25]. Here, in a first stage, parameters influencing the temperature of the collection filter were investigated. Fuel flow rate, composition and flow rate of the dispersion gas, precursor flow rate, precursor solvent, and flame dilution were adjusted. It turned out that the three major parameters defining the temperature of the collection filter (T_{coll}) were precursor flow rate (positive combustion enthalpy by organic solvents and cooling effect of non-combustible water), fuel flow rate, and aerosol dilution and cooling by environmental air. Under highly diluted conditions, T_{coll} remained below 250–270 °C and the produced powders were all amorphous despite showing different color shades and particle sizes. On the other hand powders collected above that temperature were crystalline but showed a significant loss of SSA (Table 2).

The evolution of particle size is presented as a function of the reciprocal absolute temperature T_{coll}^{-1} (K^{-1}) in Fig. 4. Particle size decreases linearly as a function of T_{coll}^{-1}. d_{BET} gently increases with increasing temperature below 260 °C. This is a common feature in flame spray synthesis: particle size increases in the flame with increasing precursor flow rates $\dot{V}_{pr}$ due to the increased cation concentration [34], which subsequently increases the flame temperature and eventually the collection site temperature. With increasing temperature, a steeper slope in d_{BET} is observed in the range of $T > 270$ °C, due to: (i) higher precursor concentration in the flame leading to higher d_{BET}; (ii) more pronounced particle growth on the filter due to the higher filter temperature T_{coll}, i.e.

Table 2
Properties of several samples of $BiVO_4$ nanoparticles made in the flame.

Sample	$\dot{V}_{pr}$ (mL min^{-1}) [a]	$\dot{m}$ (g h^{-1}) [b]	$\dot{V}_{O_2}$ (L min^{-1}) [c]	T_{coll} (°C) [d]	S_{BET} (m^2 g^{-1}) [e]	d_{BET} (nm) [f]	d_{XRD} (nm) [g]
BiV165 [h]	5.0	14.6	50 [i]	165	59	15	Amorphous
BiV203	1.0	2.92	25	203	74	12	Amorphous
BiV230	4.0	11.7	25	230	57	15	Amorphous
BiV245 [h]	10.0	29.2	25	240	31	28	Partially amorphous
BiV250	8.0	23.3	30	250	46	19	Amorphous
BiV255	8.0	23.3	35	255	45	19	Amorphous
BiV270	8.0	23.3	25	270	35	25	24.8
BiV272 [h]	10.0	29.2	25	272	24.4	35	28.1
BiV275	2.5	7.29	25	275	39.5	22	18.9
BiV289	18.0	52.5	25	289	21.6	40	32.6
BiV304	12.0	35.0	25	304	21.6	40	30.4
BiV320	24.0	70.0	25	320	17.5	49	35.9
BiV346	30.0	87.5	25	346	14.3	60	39.2
BiV300a	–	–	–	300 [j]	39	22	26.7
BiV500a	–	–	–	500 [k]	9.6	90	44.5

[a] Liquid precursor flow rate.
[b] Production rate of $BiVO_4$.
[c] Dispersion oxygen flow rate.
[d] Temperature of the collection filter.
[e] BET-specific surface area, uncertainty is ±5%.
[f] BET-equivalent diameter of monodisperse, spherical particles, uncertainty is ±5%.
[g] Crystallite diameter calculated from Scherrer equation for crystalline samples, uncertainty is ±10%.
[h] Samples prepared with a different capillary, hence their somewhat outlying properties.
[i] Oxygen replaced by air as dispersion gas.
[j] Temperature of annealing post-treatment for 15 min of a powder initially collected at 165 °C (*BiV165*).
[k] Temperature of annealing post-treatment for 4 h of a powder initially collected at 289 °C (*BiV289*).

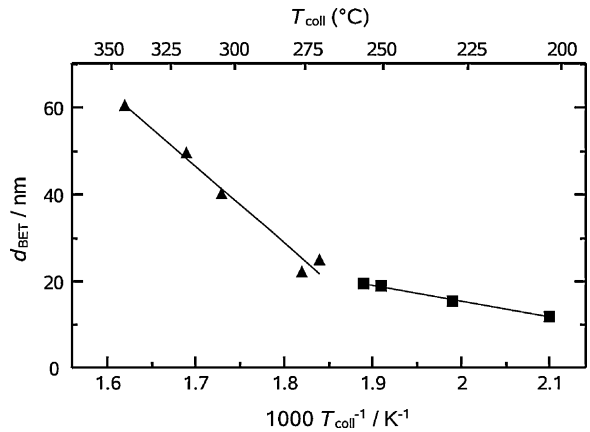

Fig. 4. BET-equivalent particle diameter (d_{BET}) of amorphous (■) and crystalline (▲) $BiVO_4$ as a function of collection filter temperature.

higher coalescence rates; (iii) better crystallinity may also trigger crystalline growth on the filter onto adjacent, very small, amorphous particles. These three phenomena cannot be distinguished in the present case. Phenomena (ii) and (iii) are likely due to thermal activation on the filter and are part of one single process where atoms are excited enough to rearrange into more ordered positions. Powders collected at the temperature where the two slopes intersect ($T_{coll} \simeq 265$ °C) have their BET-equivalent particle size (d_{BET}) equal to their crystal size (d_{XRD}), indicating that they consist of monocrystalline particles. Fig. 5 shows how crystallite size evolves with respect to particle size. Particles from synthesis conditions which resulted in a $d_{BET} < 20$ nm were amorphous and no crystal size could be calculated. Synthesis conditions resulting in d_{BET} about 25 nm are connected to a high enough collection temperature to let them crystallize completely. The ongoing increase in d_{BET} is then related to coalescence and crystallization. While d_{BET} increases faster than d_{XRD} as temperature is further increased, it is suggested that these particles are composed of multiple crystals and are therefore polycrystalline and partially aggregated (see Fig 9).

It is emphasized that all powders showing crystallinity were *only* obtained by *in situ* crystallization during collection. Attempts to modify temperature profiles of the flame cannot be successful to afford crystallization within the flame. This can be explained by the

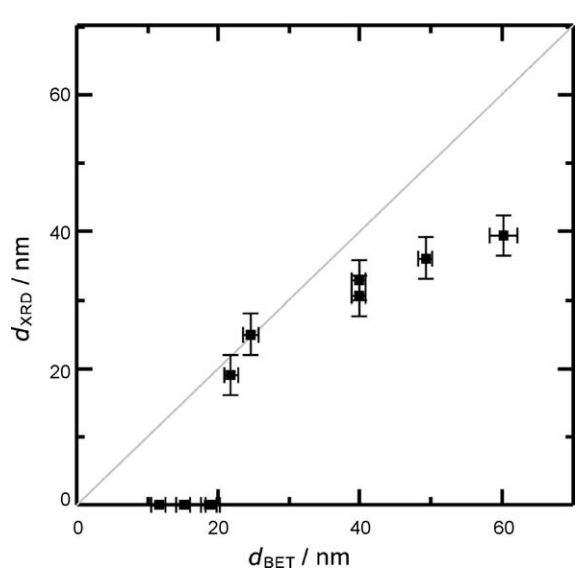

Fig. 5. Crystallite size as a function of BET-equivalent diameter.

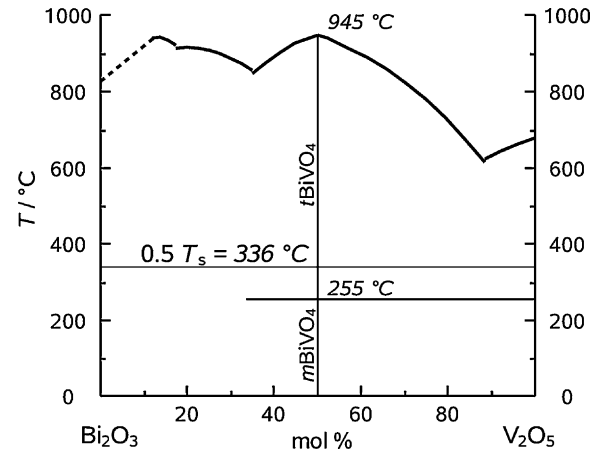

Fig. 6. Phase diagram of the Bi_2O_3–V_2O_5 system. Adapted from Ref. [38]. $BiVO_4$ exhibits the highest solidification temperature (T_s) of all compounds of the system. Therefore segregated precipitation of phases other than $BiVO_4$ is very unlikely. The ferroelastic phase transition occurs at $T_c = 255$ °C and the Tammann temperature is estimated to $T_{Tammann} = 336$ °C.

phase diagram of $BiVO_4$ (Fig. 6). Indeed the solidification temperature of $BiVO_4$ ($T_s = 945$ °C) is much lower than that of most oxides that have been previously prepared in a crystalline form by flame processes. Flame spray synthesis is known for its high maximum temperatures (2500–3300 °C) and high quenching rates (>250 000 K s^{-1}) [26]. The residence time for $T < T_s$ is too short to enable a long range ordering of the atoms into the desired scheelite structure. Silica, and other oxides with low T_s, are typically obtained in an amorphous state in a flame through fast quenching [27]. These supercooled materials behave like glasses and crystallization is hindered. Similar effects happen for $BiVO_4$ and other Bi-containing materials [35]. As a matter of fact, the influence of cooling rates in the formation of Bi and V-based oxide glasses has been studied [36,37].

In order to better understand the thermal behavior of $BiVO_4$ powders on the filter surface, calorimetric analyses (DSC) were performed. The only notable feature is a strong exothermic peak for the amorphous powder at 313 °C (Fig. 7). This peak ($T_{onset} = 302$ °C) is ascribed to the crystallization of the powder as no signal was observed at that temperature in neither the *in situ*-crystallized sample, nor in the annealed one. The $mBiVO_4 \rightleftharpoons tBiVO_4$ ferroelastic transition was not observed in the crystalline samples as it reportedly involves little thermal energy [39].

The dependence of sintering over temperature is usually described by the Tammann temperature T_{Tamman}, which is related to the melting point T_s of a solid [40,41]:

$$T_{Tamman} = 0.5T_s \quad \text{or} \quad \frac{2}{3}T_s \tag{3}$$

When this temperature is reached, atoms from the bulk will exhibit mobility. This is required for the structure rearrangement that eventually leads to crystallization, but is also responsible for coalescence. The Tammann rule has been rationalized to show that T_{Tamman} is related to a defect concentration avalanche, itself related to ionic mobility. The defect concentration $x_{\pm}$ (i.e. atomic vacancies) follows a Van't Hoff type equation:

$$\ln x_{\pm,\text{ideal}} = -\frac{\Delta H^0}{2RT} + \frac{\Delta S^0}{2R} \tag{4}$$

until the concentration becomes high enough to allow defects to perceive each other. At that point (T_{Tamman}) the concentration starts diverging overexponentially from its ideal behavior, hence launching the avalanche[41].

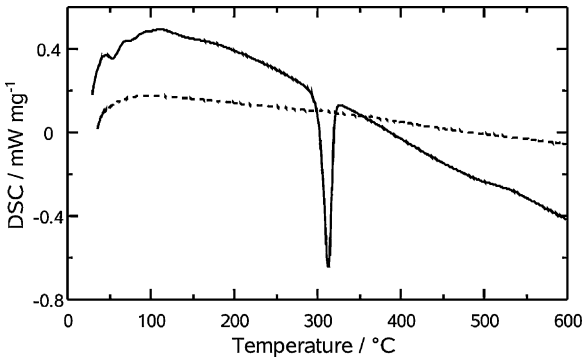

Fig. 7. DSC curves of amorphous (*BiV165*, solid line) and *in situ*-crystallized (*BiV272*, dotted line) $BiVO_4$ powders. *BiV500a* curve is identical to *BiV272*.

The informations gathered from Figs. 4 and 7 suggest that the atomic mobility (associated with O^{2-} anions) at temperatures between 250 and 350 °C within $BiVO_4$ small particles is sufficient to induce the crystallization of amorphous $BiVO_4$ into the (monoclinic or tetragonal) scheelite structure as a first step; and sintering of crystallized particles as a second step. The estimation of the Tammann temperature through Eq. (3) is plotted in the phase diagram of $BiVO_4$ (Fig. 6). The fact that the temperature at which mobility occurs also depends on texture, size and morphology can explain the lower critical values (265 and 313 °C from Figs. 4 and 7, respectively) found in this work. The 48 °C difference between these two values must arise from the experimental setup. Flame-made particles have a totally opposite temperature history because they are initially formed at very high temperature while in the DSC experiment, a cold amorphous powder was heated progressively.

Strobel et al. proposed to embed the $BiVO_4$ nanoparticles within a silica coating to keep the nanoparticles apart during the *in situ* crystallization and thus prevent sintering [25]. This approach yielded smaller primary particles than without silica and suits size requirements of the pigment industry. However, in the field of TiO_2 photocatalysis, silica coating of nanoparticles has been shown to be detrimental for electron transfer reactions [42].

3.1.2. Particle size and crystallinity

As shown in the previous section, powder quality is governed by the collection filter temperature. In turn T_{coll} depends on the dilution of the aerosol for a set of given synthesis parameters. The correlations between precursor and oxygen dispersion flow rates with T_{coll} and particle sizes and crystallinity are presented below.

Control of the process parameters of the FSS generally allows to tailor the characteristics (e.g. SSA and morphology) of the dry product particles [34,27]. Two process parameters have been investigated: (i) the precursor volume flow rate $\dot{V}_{pr}$ from 1.0 to 30.0 mL min^{-1} and (ii) the volume flow rate of dispersion oxygen $\dot{V}_{O_2}$ fed through the center outlet from 25 to 35 L min^{-1}. In the first case the oxygen flow rate was kept constant at 25 L min^{-1} and in the latter study the precursor volume flow rate was always 8.0 mL min^{-1}. The properties of selected $BiVO_4$ powders prepared by FSS are summarized in Table 2.

Amorphous powders collected in the temperature range $T_{coll} < 270$ °C show particle sizes (d_{BET}) between 12 and 19 nm. The smallest particle size was obtained by spraying the precursor at $\dot{V}_{pr} = 1$ mL min^{-1}, i.e. particle size can be conveniently decreased by lowering $\dot{V}_{pr}$. When $\dot{V}_{pr}$ was fixed to 8 mL min^{-1} and dispersion oxygen flow rate was varied from 25 to 35 L min^{-1}, the collection filter cooled down from 270 to 250 °C. The main feature observed in this range of $\dot{V}_{O_2}$ values is the change from *crystalline* $BiVO_4$ ($\dot{V}_{O_2} = 25$ L min^{-1}; $T_{coll} = 270$ °C) to *amorphous* $BiVO_4$ ($\dot{V}_{O_2} = 30$ L min^{-1}; $T_{coll} = 255$ °C). If the two *amorphous* samples of this series are compared (*BiV250* and *BiV255*), it turns out that $\dot{V}_{O_2}$ has little or no influence on particle size since both show the same $d_{BET} = 19$ nm.

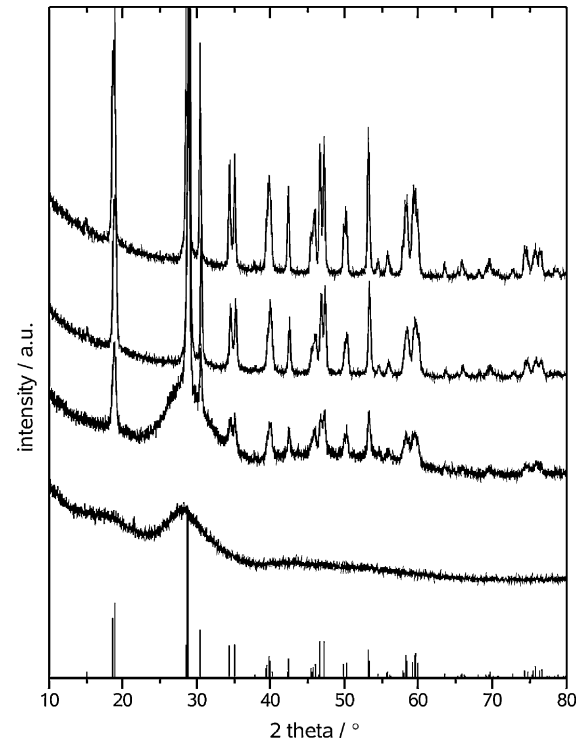

Fig. 8. XRD patterns of selected $BiVO_4$ powders. From bottom to top: PDF 83-1700 (Powder Diffraction File, release 2001), amorphous *BiV165*, partially crystalline *BiV245*, crystalline *BiV289*, highly crystalline *BiV500a*.

In the range $270 < T_{coll} < 350$ °C, the obtained powders were always *crystalline* and particle size d_{BET} varied between 22 and 60 nm for precursor flow rates between 8 and 30 mL min^{-1}. All the amorphous and crystalline flame-made particles are in the nano-domain ($d < 100$ nm) and have a specific surface area (SSA) higher than 10 m^2 g^{-1} (Table 2), i.e. more than one order of magnitude higher than those $BiVO_4$ particles made through other synthesis routes (Table 1). In solid state reactions for instance, diffusion of one oxide into the other one has to be reached, what happens at rather high temperatures and is connected with a high loss of surface area.

3.1.3. Crystalline phase and morphology

The XRD patterns of the $BiVO_4$ nanoparticle samples produced by FSS reveal the diffraction profile of clinobisvanite with the main triplet peak at 28.8°.[1] Peaks of segregated pure oxide phases of the single components are not observed. This is not surprising since Bi_2O_3 and V_2O_5 – as well as other intermediate phases – have lower solidification temperatures T_s than $BiVO_4$ (Fig. 6). This is an important issue because phases with undesired stoichiometry may form when the solidification temperature of a given oxide is much higher than that of the desired one. The diffractograms of three powders collected at different temperatures and one further annealed sample (as reference) are shown in Fig. 8. The powder prepared at low T_{coll} (here *BiV165*) is amorphous. The diffractogram of the sample with severe annealing post-treatment (*BiV500a*) is used as reference for a highly crystalline sample.

[1] ICSD entry # 100602 (monoclinic symmetry, S.G *I*2/*b* No. 15, unit-cell parameters $a = 5.1935(3), b = 5.0898(3), c = 11.6972(8), \gamma = 90.387(4)°$, $V = 309.2$ Å^3) [43].

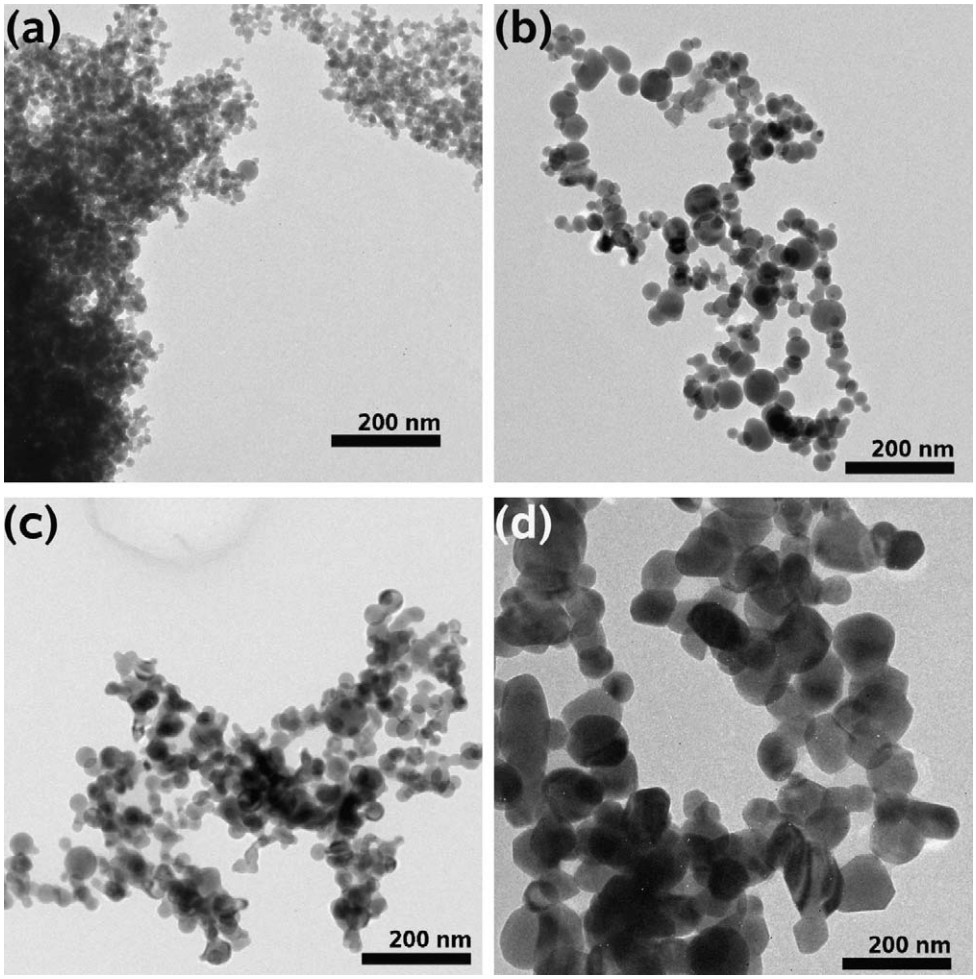

Fig. 9. TEM micrographs of: (a) amorphous *BiV165*, (b) partially crystalline *BiV245*, (c) crystalline *BiV272*, (d) highly crystalline *BiV500a*.

The pattern of *BiV289* is very similar to the latter one so that it can be considered as *fairly crystalline*. *BiV245* shows well defined diffraction peaks but does also contain features of amorphous powders. Crystal size (d_{XRD}) was calculated for each crystalline sample after Rietveld refinement using Scherrer's equation and are listed in Table 2.

Rietveld refinement was also used to determine the lattice constants of the crystalline powders. Unit-cell parameters of *in situ*-crystallized *BiV289* nanoparticles are $a = 5.1943(3), b = 5.0990(3), c = 11.7010(6), \gamma = 90.351(4)$ and $V = 309.90(4)$ Å^3. The annealing post-treatment carried out on *BiV289* did not affect its cell parameters: $a = 5.1904(2), b = 5.0943(2), c = 11.6958(4)$, $\gamma = 90.338(2)$ and $V = 309.25(3)$ Å^3. As expected from the diffraction patterns, these cell parameters are in a very good correlation to those of mBiVO$_4$ [43].

The amorphous-to-crystalline transition deserves special attention. From what has been discussed previously, it appears that $T_{coll} = 265\,^{\circ}$C is a critical temperature for the *in situ* crystallization. The authors believe this is directly connected to the Tamman temperature and somehow to the ferroelastic transition of BiVO$_4$, which occurs at $T_c = 255\,^{\circ}$C (Fig. 6) [44]. Between 255 and 945 °C, BiVO$_4$ exists in a solid, tetragonal phase (tBiVO$_4$) where Bi atoms lie in the middle of a regular square antiprism [45]. Nanoscale, amorphous flame-made BiVO$_4$ particles may rearrange to tBiVO$_4$ at temperatures slightly higher than T_c. Atoms may have a higher tendency to rearrange because of the small size of the particles ($d_{BET} < 20$ nm). In nanoparticles, there is a high relative number of surface atoms with dangling bonds willing to adopt more favored positions and this may contribute to lower $T_{Tammann}$. The crystallization process seems to proceed at lower temperatures for nanoparticles than it does at the macroscopic scale for this reason, as suggested in another field [46]. When powders collected at temperatures $T_{coll} > T_c$ are cooled down, the *in situ*-crystallized tBiVO$_4$ phase undergoes the ferroelastic transition to relax to the desired mBiVO$_4$ phase (*distorted* square antiprism).

A TEM micrograph of amorphous BiVO$_4$ nanoparticles (*BiV165*) is shown in Fig. 9a. They show typical features of flame-made nanoparticles like nanoscale, spherical shape, narrow size distribution and low degree of aggregation [34]. Samples *BiV245* and *BiV272* are presented in Fig. 9b and c, respectively. Particle sizes are consistent with those determined by BET analysis. Furthermore, the microstructural analysis by TEM revealed that the higher T_{coll} had no major impact on the degree of aggregation and both samples exhibit spherical particles. The impact of the crystallization process on the filter is limited to a minor formation of sinternecks, but no effect on the particle size by particle growth is observed. This correlates well with the above-mentioned d_{BET} and d_{XRD}. The morphology of the reference material *BiV500a* including additional annealing post-treatment at 500 °C for 4 h can be seen in Fig. 9d. In addition to the obvious larger primary particle size, a clear difference in particle morphology can be seen: particles are not spherical but polyhedral. The annealing step has provided sufficient energy to let facets grow and rearrange to a more favorable crystal shape. This particular morphology is observed for most synthesis routes, in which an additional annealing step is included [6,24]. Furthermore, aggregation is much more significant

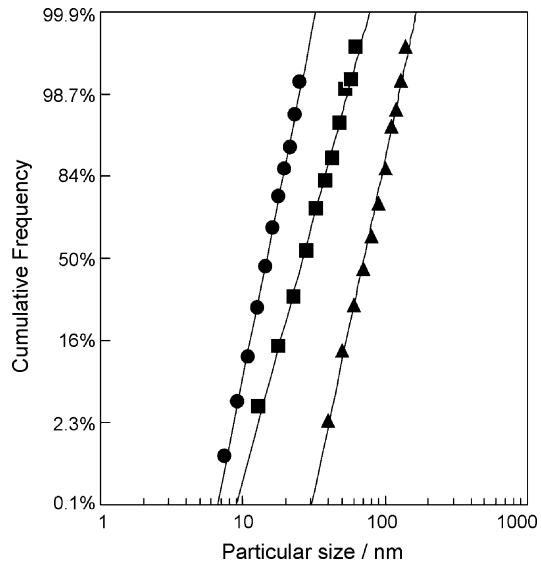

Fig. 10. Particle size distribution of amorphous *BiV165* (●) with $d_{50} = 14.7$ nm and standard deviation $\sigma_g = 1.30$; crystalline *BiV272* (■) with $d_{50} = 26.4$ nm, $\sigma_g = 1.43$; *BiV500a* (▲) with $d_{50} = 69.9$ nm, $\sigma_g = 1.35$.

for this annealed sample than for non-annealed ones. Therefore, the *in situ*-crystallized sample has the advantage to present smaller and less-aggregated particles.

A more detailed analysis was carried out to find particle size distribution from TEM images and is presented in Fig. 10. The standard deviation σ_g, is a crucial parameter for the width of a distribution and reflects also the quality and homogeneity of the synthesis process. It can be seen that the *in situ* crystallization leads to a particle growth from a $d_{50} = 14.7$ (*BiV165*) to 26.4 nm (*BiV272*) and also that σ_g increased from 1.3 to 1.45. Both latter values are in the range of typical values for flame-spray-made powders since typical geometrical standard deviations, e.g. from nebulizers, are in the range of 1.7 and higher [47].

The severe annealing post-treatment lead to a significant increase of particle size. A $d_{50} = 70$ nm was determined for the *BiV500a*, with a σ_g of 1.35. Average particle sizes d_{TEM} of *BiV165* and *BiV272* fit well to d_{BET} of amorphous and crystalline samples, respectively (Table 2). The deviation from d_{TEM} to $d_{XRD} = 44.5$ nm and $d_{BET} = 90$ nm for *BiV500a* is typical for annealed samples, and reflects interstitial particle necking of the primary particles and the fact that particles can consist of several crystal units.

3.1.4. Surface electric charge

Fig. 11 shows ζ potential curves as a function of pH. The isoelectric point (IEP) of *BiV304* is 2.3, quite close to the 2.7 value

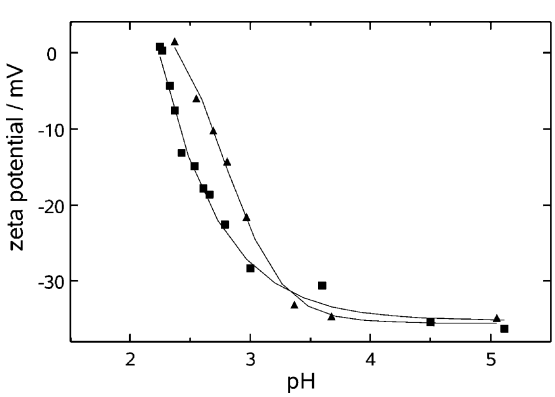

Fig. 11. ζ potential as a function of pH of flame-made $BiVO_4$ (sample *BiV304*) with *in situ* crystallization (■) and with annealing post-treatment (▲).

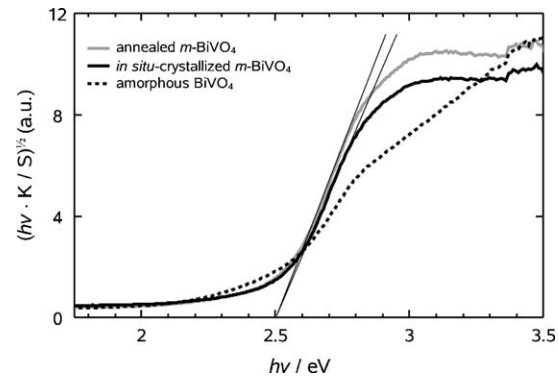

Fig. 12. Absorption spectra of Flame Spray-made $BiVO_4$ powders (*amorphous*, with *in situ* crystallization *monoclinic* and with annealing post-treatment *monoclinic*) and estimation of their band gaps (E_g). The partially crystalline powder shows a flatter profile with an absorption tail in the green region of the spectrum and poorer absorption beyond E_g.

reported by Xie et al. [12]. In contrast with the results of Strobel et al. [25], the as-prepared $BiVO_4$ nanoparticles possess surface negative charges ($\zeta < -30$ mV). This feature may explain the good ability of $BiVO_4$ to oxidize cationic dyes [7,9,10], which can adsorb electrostatically onto the photocatalyst surface, i.e. when the degradation mechanism occurs through direct hole oxidation. As a matter of fact, adsorption through the dialkylamine moiety on negatively charged TiO_2 has been reported by the group of Zhao for MB [48] and sulforhodamine-B [49] prior to oxidation.

3.2. Optical properties

Diffuse reflectance spectra (DRS) confirmed that all samples absorb visible light. The nature of the electronic transition in mBiVO$_4$ upon light absorption has been suggested as an indirect transition owing to the Bi^{3+} stereoactive lone pair breaking the symmetry of the VO_4^{3-} tetrahedron [45]. Therefore $\sqrt{h\nu(K/S)}$ was plotted *vs.* $h\nu$ to obtain a bandgap estimate of the *indirect* transition [50]. As expected from the monoclinic phase identified by XRD, all crystalline samples (both with *in situ* crystallization and annealing post-treatment) show a sharp optical absorption bandgap at 2.50 eV (496 nm), which confirms the bright yellow color of the powders (Fig. 12). Less crystalline and amorphous powders show gentler absorption profiles and absorption tails into longer wavelengths (i.e. lower energies), in agreement with orange and even brown colors observed in these samples.

Non-pure bandgap absorption is caused by structure defects. This phenomenon is sought in e.g. N-doped TiO_2, where visible response is obtained by the modification of a UV-active semiconductor [32,51]. However, these defects also increase charge recombination and this is one of the reasons why high crystallinity is beneficial for good photocatalytic activity. $BiVO_4$ is intrinsically visible light-active: impurity levels are not only superfluous here but even undesired. Kudo et al. attributed the tails of the light absorption profile to recombination-favoring defects [6], which are intrinsically present in amorphous materials. Absorption spectrum profiles can thus be related to crystallinity. The authors recommend considering the steepness of the absorption profiles to estimate the degree of crystallinity as a complement to diffraction profiles. Indeed peak broadening can be caused by a number of factors beyond crystallinity.

The optical properties of an oxide depend on surface modifications caused by the environment. The best known phenomenon is the reversible addition or withdrawal of oxygen atoms caused by changes in oxygen partial pressure. In the present work, drying of powders at 180 °C under N_2 flow (reducing atmosphere) induced a strong color change. Powders became vivid

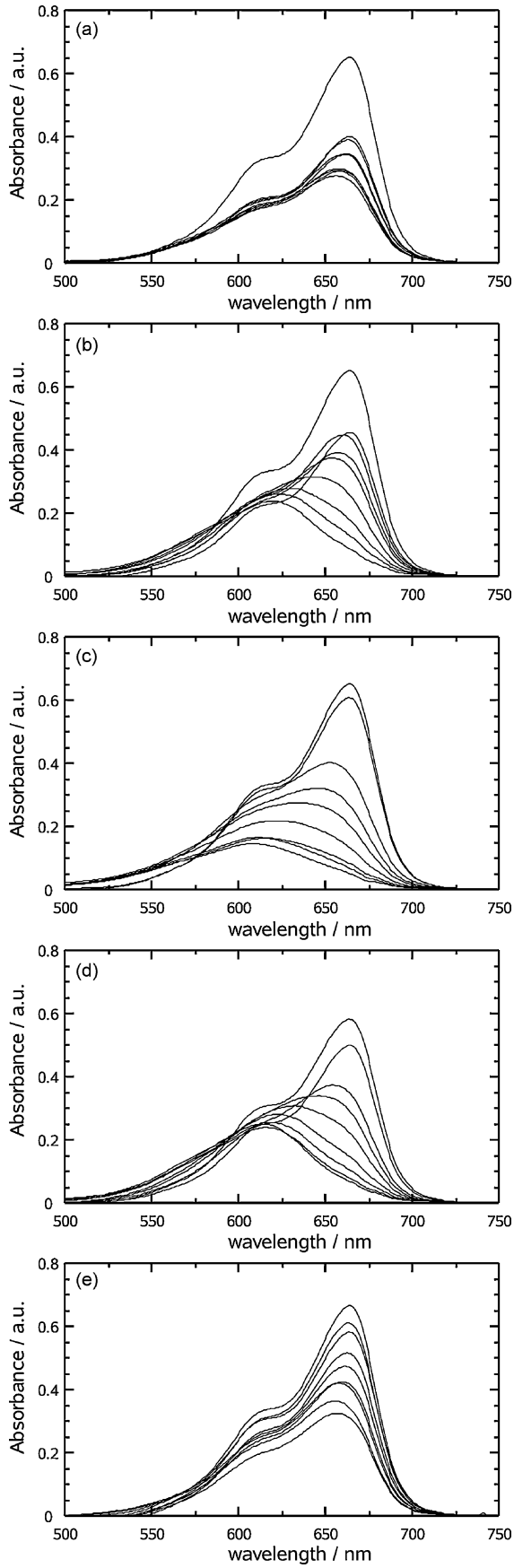

Fig. 13. Vis spectra of a stirred 10^{-5} M MB, air-saturated, aqueous solution in a 1 cm spectrophotometer cell after centrifugation of the 0.1 g L^{-1} $BiVO_4$ slurry: (a) *BiV165*; (b) *BiV272*; (c) *BiV500a*; (d) *BiV300a*; (e) P25. The spectra were recorded at the following visible-light (5.8 mW cm^{-2}) irradiation times (from top to bottom): -15, 0, 10, 30, 60, 120, 180, 240, 300 min. Initial pH: 5.5.

green along the process and kept this new color once they were cooled to ambient temperature so that a thermochromic effect can be ruled out. They eventually recovered their original vivid yellow color after several days of contact with ambient air or when poured into water. This phenomenon is ascribed to an oxygen depletion that causes severe under-stoichiometry [52]. Oxygen vacancies have been held responsible for absorption red shift in TiO_2[53,54] and the authors suggest the same reversible behavior is observed for the powders presented in this work. The varying degree of oxygen vacancies could also explain all the different hues reported for $BiVO_4$ prepared by different methods and with a different temperature history. In this work, less crystalline samples showed more intense color changes. This may be interpreted in terms of surface energies with oxygen atoms having more freedom to move around and be withdrawn. This is because their binding energies are expected to be lower when they belong to an amorphous structure.

3.3. Photocatalytic activity towards methylene blue

Photocatalytic activity of flame-made $BiVO_4$ nanoparticles was tested towards the degradation of an aerated, aqueous solution of methylene blue (MB) under blue light irradiation ($400\,nm < \lambda < 500\,nm$, see Fig. 2). The redox chemistry of MB in the frame of TiO_2 photocatalysis was reviewed by Mills and Wang [55]. In the present study the absorbance at 664 nm was monitored upon irradiation time to estimate the disappearance of MB.[2]

3.3.1. Degradation at pH 5.5

Fig. 13 shows the visible absorption spectra of aqueous solutions of MB after several times of irradiation in presence of amorphous, *in situ*-crystallized, and (severely and mildly) annealed $BiVO_4$. Absorbance readily decreases about 40% from 0.65 to 0.40 in the suspension of *BiV165* upon adsorption in the dark (Fig. 13a). This is ascribed to the high SSA of this powder ($59\,m^2\,g^{-1}$), one of the main features aimed in this work, since adsorption is the first step required in a heterogeneous catalytic reaction. However, the decrease in absorbance at 664 nm under irradiation is very weak (0.40–0.26 a.u.); a minor blue-shift of the peak is observed down to 656 nm. The adsorption effect is similar for the more crystalline *BiV272* (Fig. 13b). Upon irradiation, the peak at 664 nm progressively shifts to lower wavelengths (hypsochromic effect). It is worth to note that while absorbance at 664 nm strongly decreases, absorbance at about 615 nm remains almost constant after the adsorption step. This is due to the overlap of two peaks: a shoulder observed in pure MB solutions at 612 nm due to the dimerized form of the dye [56] (Fig. 13: uppermost curves); and the build-up of the signal caused by the *N*-demethylation products of MB [48], with Azure A, B and C absorbing on the 608–655 nm range and stronger shift representing higher degree of demethylation [57,58]. The spectra of the solution containing the severely annealed $BiVO_4$ powder are identical at times $t = -15$ min and $t = 0$ as adsorption is negligible (Fig. 13c).

Poor adsorption on *BiV500a* does not appear as a major drawback for MB degradation as the main absorption peak undergoes a significant decrease besides a strong hypsochromic effect (Fig. 15a). Furthermore, the peak about 615 nm constantly decreases, indicating that the demethylated intermediates do not accumulate upon formation and must undergo a ring cleavage that

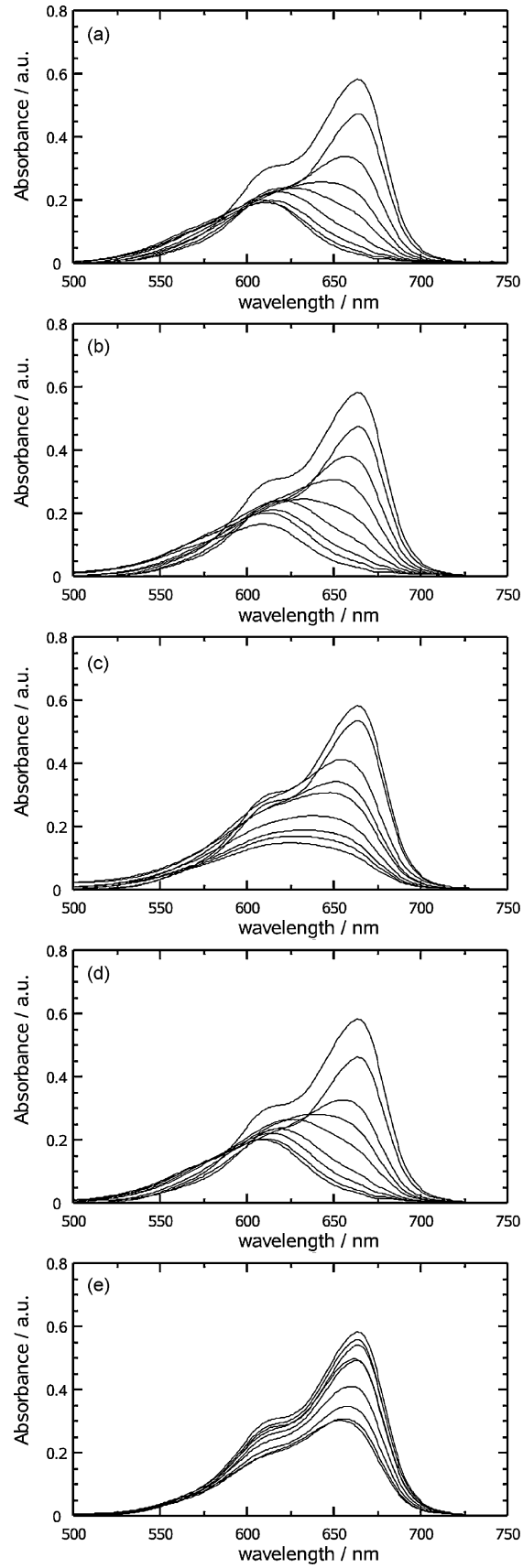

Fig. 14. Vis spectra of a stirred 10^{-5} M MB, air-saturated, aqueous solution in a 1 cm spectrophotometer cell after centrifugation of the 0.1 g L^{-1} $BiVO_4$ slurry: (a) *BiV165*; (b) *BiV272*; (c) *BiV500a*; (d) *BiV300a*; (e) P25. The spectra were recorded at the following visible-light (5.8 mW cm^{-2}) irradiation times (from top to bottom): −15, 0, 10, 30, 60, 120, 180, 240, 300 min. Initial pH: 8.5.

[2] In the current subsection, *degradation* refers to whatever *irreversible* chemical transformation of MB, which may include amine dealkylation, aromatic ring cleavage or other oxidation processes. The term *decolorization* describes an absorbance drop of the typical absorption spectrum of MB. It can originate either from an oxidative, *irreversible* ring cleavage or from a *reversible* reductive photobleaching.

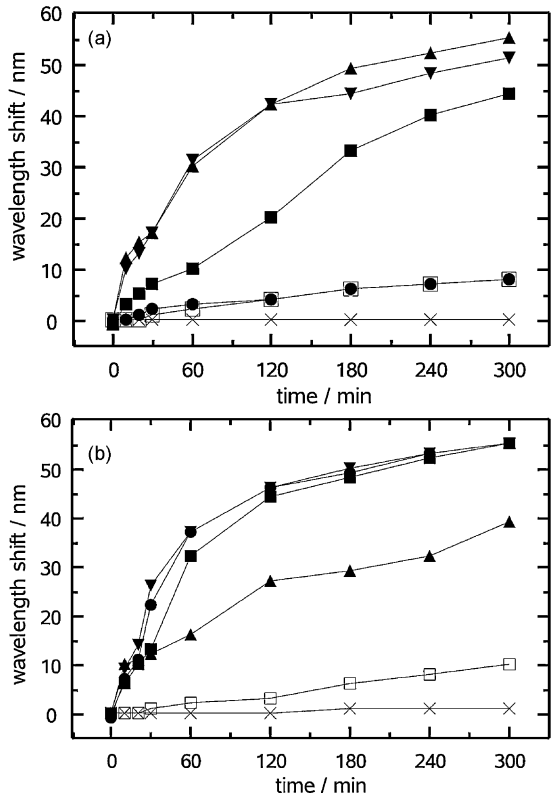

Fig. 15. Wavelength blue shifts of the 664 nm band of MB in aqueous irradiated solutions at (a) pH 5.5 and (b) pH 8.5: *BiV165* (●); *BiV300a* (▼); *BiV272* (■); *BiV500a* (▲); Degussa P25 (□); without photocatalyst (×).

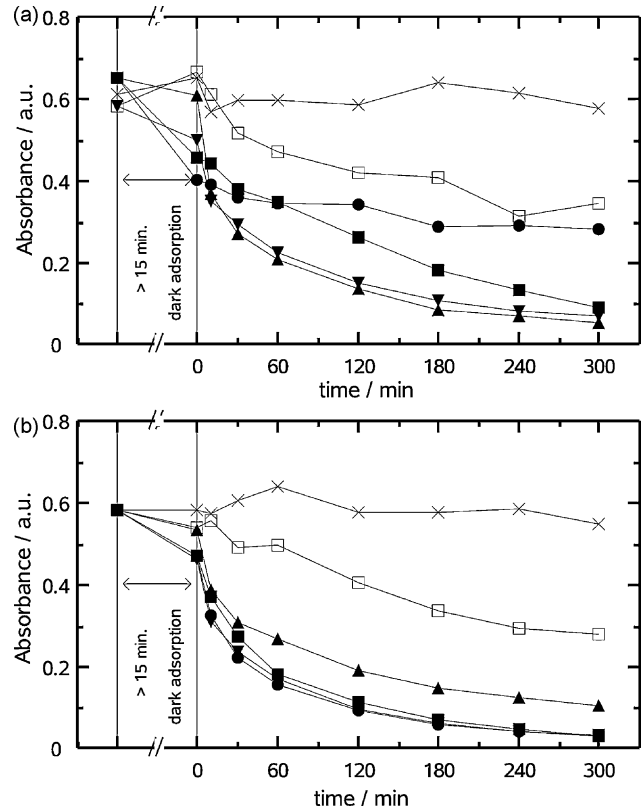

Fig. 16. Absorbance at 664 nm of centrifuged solution of MB 10^{-5} M as a function of irradiation time at (a) pH 5.5 and (b) pH 8.5: *BiV165* (●); *BiV300a* (▼); *BiV272* (■); *BiV500a* (▲); Degussa P25 (□); without photocatalyst (×). The change in absorbance before irradiation is due to adsorption in the dark.

implies the destruction of the chromophoric structure in a manner similar to that reported by Herrmann and coworkers [59]. The very weak adsorption onto this annealed photocatalyst may result from the much lower SSA (9.6 $m^2\,g^{-1}$) or from chemical modification (e.g. surface dehydroxylation) after the annealing process.

The second annealed sample, i.e. *BiV300a*, shows mild adsorption under dark conditions (Fig. 13d) but rapidly achieves high decolorization with a strong hypsochromic shift (613 nm) similar to *BiV500a* (Fig. 15a). However, the end-of-run spectrum has a sharper peak, reminiscent of Fig. 13b (the other crystalline sample with moderately high SSA). Demethylation seems to proceed quickly with these two samples but it results in an accumulation of the demethylated species that could be recalcitrant to ring cleavage.

The absorption spectra of a solution containing Degussa P25 are presented for comparison (Fig. 13e). The profiles keep the same pattern along the whole irradiation run with a decrease in intensity of about 50% from 0.68 to 0.36 a.u. The main peak is only shifted to 656 nm, after 300 min, just like in the case of *BiV165*, so that intermediates of the Azure kind are not formed.

It seems that TiO_2-mediated MB photodegradation only proceeds through direct ring cleavage under visible light at pH 5.5. Visible light-mediated TiO_2 photocatalysis has been reported for some types of charge transfer (CT) complexes on TiO_2 surfaces with e.g. phenol [60], ascorbic acid [61] and H_2O_2[62], but also by adsorbed dye photosensitization [63]. These processes are related to specific LMCT and degradation pathways so that single types of oxidation can be favored (e.g. ring cleavage over dealkylation or *vice versa*). This was shown in the elegant work by Zhao and coworkers on sulforhodamine-B, where the two degradation pathway could be controlled by the mode of adsorption of the dye [49].

In the present study, it remains unclear whether the degradation is caused by the absorption of visible light by complexes of the above-mentioned type (and not by the bulk semiconductor) or by the very weak overlap of the absorption spectrum of anatase and the emission spectrum of the lamp at 400 nm (Fig. 2). The absence of demethylation is rather uninformative over this point since the two mechanisms have been observed in traditional TiO_2 UV photocatalysis over a wide range of pH [48,59].

The decolorization of a MB solution can also occur through a reversible reductive photobleaching. But the injection of oxygen suppresses the possibility to find reduced species of MB [55]. Injection of compressed air into the UV–vis cuvette for 30 min in the dark after a 30-min-irradiation step did not affect the absorption spectrum of the solution for any photocatalyst, i.e. no color recovery was observed under any circumstance. Therefore, the observed decolorization must exclusively reflect the oxidation of MB through irreversible processes. However, the possibility that MB undergoes a transient reduction followed by a fast re-oxidation cannot be yet excluded [55].

The most striking features observed in the degradation runs carried out at pH 5.5 are summarized in Figs. 15a and 16a: failure of the amorphous $BiVO_4$ sample (*BiV165*, 59 $m^2\,g^{-1}$), and the high initial degradation rate obtained with the most crystalline sample (*BiV500a*, 9.6 $m^2\,g^{-1}$). It is noteworthy that the two annealed samples show identical wavelength shift behavior (Fig. 15a).

3.3.2. Degradation at pH 8.5

Fig. 14 shows the absorbance of MB solutions with the same photocatalysts as above but with an initial pH of 8.5.

The decrease in absorbance upon dark adsorption is the same for all $BiVO_4$ photocatalysts but *BiV500a*. When the light is switched on, they show the same behavior (Fig. 14a, b and d), i.e fast absorbance decrease and strong hypsochromic shift to exactly 609 nm after 300 min. The two samples with highest SSA (*BiV165* and *BiV300a*)

show the fastest shift after 30 min (Fig. 15b). In the case of *BiV272* and *BiV300a*, the patterns are very similar to those observed at pH 5.5. *BiV165*, in turn, did not show significant activity at pH 5.5.

It is worth to note that the curves remain almost identical for this sample with $A_{max} = 0.20$ at 610 nm after 180, 240 and 300 min (Fig. 14a). This behavior shows either some kind of poisoning or that full demethylation of all MB molecules has been achieved and the incapacity of amorphous $BiVO_4$ to further oxidize the demethylated chromophoric structure. The latter option seems more realistic because identical shift is reached with three photocatalysts with quite different SSA (Table 2).

BiV500a shows a weaker absorbance decrease at 664 nm (Fig. 16b) and a weaker blue shift (Fig. 15b), which results in a very broad final single peak: with $A_{624} = 0.15$ a.u. (Fig. 14c).

The broad peaks observed at the end of the runs for *BiV500a* under both pH conditions prove the coexistence of Azure intermediates with different degrees of demethylation. The fact that the last four spectra (120, 180, 240, 300 min) have similar shapes, i.e. similar shifts, and decreasing intensities suggests that ring cleavage is favored over demethylation at the end of the run for this lower SSA photocatalyst.

P25 shows some activity (Fig. 14e) but at a much lower rate than the $BiVO_4$ photocatalysts. As observed for the solution at pH 5.5, the hypsochromic shift is negligible so that degradation must exclusively occur through ring cleavage.

What is most impressive in this set of experiments at pH 8.5 is the high activity of *BiV165* as one of the best photocatalyst in terms of demethylation despite its lack of crystallinity (Fig. 15b). This behavior was somehow recently reported by Yu et al. without further details on pH conditions nor on the aspect of the spectra [10]. In sight of this rapid demethylation, it should be spoken of conversion rather than degradation because of the accumulation of the final Azure intermediate. It seems that demethylation is favored by high SSA photocatalysts regardless of their crystallinity (samples *BiV165*, *BiV300a*, *BiV272*), whereas ring cleavage does require high crystallinity. This is illustrated by the highest absorbance decrease shown by *BiV500a* (Fig. 14c).

These observations show that amorphous $BiVO_4$ nanoparticles are able to carry out the demethylation of MB. This might be extended to the dealkylation of other amino groups. The "decomposition" of MB with amorphous $BiVO_4$ reported by Yu et al. may also have been a simple demethylation with no destruction of the aromatic structure [10]. This could explain the failure of that material to evolve O_2. In that work, only crystalline materials were able to evolve O_2. This is not so surprising since both O_2 evolution and OH generation on a semiconductor surface result from H_2O oxidation. In sight of the application to industrial wastewater remediation, demethylation may not be regarded as an advanced oxidation process (AOP) since the stable aromatic thionine structure remains unaffected. The photocatalytic reaction could rather be regarded as a selective transformation of MB into thionine or one of the Azure dyes. For instance, Azure A, B and C were recently selectively synthesized from MB by plant peroxidases [64]. More precise identification of the intermediates produced in this work is under investigation.

The impact of pH in the degradation is not well understood. It seems that adsorption during the pre-irradiation time is weaker at pH 8.5 (Fig. 16). The change in pH mainly changes the surface charge of the semiconductor surface but the most significant changes occur when moving across the IEP, which in the present case lies much lower (2.3) than the studied pH range.

The singular behavior of *BiV165* is not understood but it is proven that demethylation is strongly inhibited at pH 5.5. On the other hand *BiV500a* shows little less demethylation at pH 8.5 Nevertheless, different pollutants behave in a different manner in presence of photocatalysts with different sizes, crystallinities and IEP [65]. Future work will show how surface area and crystallinity of $BiVO_4$ photocatalysts affect their activity in interaction with other pollutants.

Finally, removal of total organic carbon (TOC) after 300 min was only significant for *BiV500a* at both pH values (TOC removal $\simeq 25\%$). This indicates that although partial bleaching of the MB solution can be achieved in the present system, complete mineralization of the pollutant into CO_2, NH_4^+ and NO_3^- is not attained.

3.4. Impact of the annealing post-treatment

When $BiVO_4$ nanoparticles underwent severe annealing to yield *BiV500a*, their morphology changed from regular spheres to larger polyhedron-shaped crystals (Fig. 9d). This means the surface of the photocatalyst is almost entirely dominated by energetically favored crystalline facets. Edges and vertices thus represent a negligible part of the surface. Heterogeneous catalytic reactions are known to be highly dependent on the reaction sites or structure defects. These phenomena have been studied for TiO_2 in the field of photocatalysis [66]. As a matter of fact, highly reacting sites tend to occur on surface irregularities such as edges and vertices so that spherical particles seem particularly appropriate to maximize the number of kind of sites because the actual topography of a spherical particle is a constant succession of small crystalline faces, edges and vertices that give it its round appearance. In spite of these important geometrical modifications, surface charges seem not to be affected. The IEP was only shifted from 2.3 to 2.5 upon annealing and ζ potentials were almost identical along the whole range of pH.

As mentioned in Section 3.1.2, *in situ* crystallization lead to crystalline powders with an SSA roughly halved with respect to amorphous powders collected at lower temperatures. In other synthesis routes, the crystallization step through annealing often leads to more dramatic loss in BET area (see Table 1). In this work, severe annealing of an *in situ-crystallized* crystalline powder also lead to SSA loss and enhanced crystallinity. However, the SSA loss was only of a factor of 2 (Table 2). The evolution may be better understood in terms of particle size as shown in Fig. 10 by TEM size distributions. This shows that the severe annealing post-treatment of flame-made $BiVO_4$ nanoparticles yields *highly* crystalline, *nanoscale* $BiVO_4$ nanopowders. On the one hand, *high* crystallinity because annealing further crystallizes the particles and on the other hand, *nanoscale* because their size is still lower than 100 nm. On the other hand amorphous $BiVO_4$ yielded a fairly crystalline powder (*BiV300a*) with an SSA of 39 $m^2\,g^{-1}$ after a mild annealing post-treatment (300 °C, 15 min), which represents a loss of only one third of the initial SSA. This highlights the relatively low amount of energy required to drive the crystallization of amorphous $BiVO_4$ nanopowders (Fig. 7). The photocatalytic activity of this powder was comparable to that of the *in-situ* crystallized *BiV272*, so the heat-saving *in situ* treatment leads to the same result as the electric power-consuming furnace post-treatment with similar time and temperature.

The annealing post-treatment therefore appears as an optional, polyvalent tool to crystallize – or increase the crystallinity – of a wide range of flame-made $BiVO_4$ nanopowders while keeping most of their SSA. Flame-made, annealed particles remain with significant lower particle diameter than those produced by solid state reaction and also show high productions rates compared to e.g. hydrothermal routes (Table 1). By the method presented in this work, size and crystallinity were successfully controlled during the synthesis of $BiVO_4$.

4. Conclusion

The preparation of amorphous and crystalline $BiVO_4$ nanoparticles by means of flame spray synthesis has been reported for their

production as photocatalyst. In this work, *in situ*, self-sustained crystallization for the production of spherical, crystalline $BiVO_4$ nanoparticles is reported and this process can be easily scaled up. A minor particle size increase was observed during the *in situ* crystallization but this process yielded contamination-free, monoclinic $BiVO_4$ active photocatalysts without the help of phase stabilizer (dopant) or particle coating. Compared to common particle sizes from other synthesis routes, the particle size of the amorphous and the crystalline samples are about one order of magnitude smaller. High SSA amorphous $BiVO_4$ photocatalytically converted MB to Azure intermediates under basic conditions through *N*-demethylation without apparently affecting the thionine chromophoric structure. On the other hand, high crystallinity seems to remain the most important parameter for the ring cleavage of methylene blue by monoclinic $BiVO_4$ under visible light irradiation.

Acknowledgements

The authors thank the Secrétariat d'État Suisse à l'éducation et à la recherche (SER) for its support to the project SER C06.0074 in the framework of the COST Action 540 "PHONASUM" from the European community; Prof. J.-E. Moser and J. Teuscher (Photochemical Dynamics Group, EPFL) for their help in the recording of DRS spectra; Dr P. Hug (Laboratory for Solid State Chemistry and Catalysis, EMPA) for the DSC measurements; Dr Ch. Roussel (Section of Chemistry and Chemical Engineering, EPFL) for kindly providing access to UV–vis spectroscopy and ζ potential instruments; L. Ding for the IEP measurements. Dr J.A. Rengifo-Herrera contributed to fruitful discussions and experimental setups. Finally, the anonymous reviewers are thanked for their constructive criticisms and suggestions.

References

[1] B. Ohtani, Chem. Lett. 37 (3) (2008) 216–229.
[2] M.R. Hoffmann, S.T. Martin, W. Choi, D.W. Bahnemann, Chem. Rev. 95 (1) (1995) 69–96.
[3] D. Chatterjee, S. Dasgupta, J. Photochem. Photobiol. C 6 (2–3) (2005) 186–205.
[4] F.E. Osterloh, Chem. Mater. 20 (1) (2008) 35–54.
[5] A. Kudo, Y. Miseki, Chem. Soc. Rev. 38 (1) (2009) 253–278.
[6] A. Kudo, K. Omori, H. Kato, J. Am. Chem. Soc. 121 (49) (1999) 11459–11467.
[7] X. Zhang, Z. Ai, F. Jia, L. Zhang, X. Fan, Z. Zou, Mater. Chem. Phys. 103 (1) (2007) 162–167.
[8] L. Zhou, W. Wang, S. Liu, L. Zhang, H. Xu, W. Zhu, J. Mol. Catal. A: Chem. 252 (1–2) (2006) 120–124.
[9] L. Zhou, W. Wang, L. Zhang, H. Xu, W. Zhu, J. Phys. Chem. C 111 (37) (2007) 13659–13664.
[10] J. Yu, Y. Zhang, A. Kudo, J. Solid State Chem. 182 (2) (2009) 223–228.
[11] S. Kohtani, S. Makino, A. Kudo, K. Tokumura, Y. Ishigaki, T. Matsunaga, O. Nikaido, K. Hayakawa, R. Nakagaki, Chem. Lett. 31 (7) (2002) 660–661.
[12] B. Xie, H. Zhang, P. Cai, R. Qiu, Y. Xiong, Chemosphere 63 (6) (2006) 956–963.
[13] M. Long, W. Cai, J. Cai, B. Zhou, X. Chai, Y. Wu, J. Phys. Chem. B 110 (41) (2006) 20211–20216.
[14] A. Kudo, K. Ueda, H. Kato, I. Mikami, Catal. Lett. 53 (3–4) (1998) 229–230.
[15] J. Yu, A. Kudo, Adv. Funct. Mater. 16 (16) (2006) 2163–2169.
[16] S. Tokunaga, H. Kato, A. Kudo, Chem. Mater. 13 (12) (2001) 4624–4628.
[17] J. Yu, A. Kudo, Chem. Lett. 34 (6) (2005) 850–851.
[18] K. Hirota, G. Komatsu, M. Yamashita, H. Takemura, O. Yamaguchi, Mater. Res. Bull. 27 (7) (1992) 823–830.
[19] A. Galembeck, O.L. Alves, Thin Solid Films 365 (1) (2000) 90–93.
[20] A.G. Agrios, P. Pichat, J. Photochem. Photobiol. A 180 (1–2) (2006) 130–135.
[21] S. Kohtani, K. Yoshida, T. Maekawa, A. Iwase, A. Kudo, H. Miyabe, R. Nakagaki, PCCP 10 (2008) 2986–2992, and references therein.
[22] S.S. Dunkle, R.J. Helmich, K.S. Suslick, J. Phys. Chem. C 113 (28) (2009) 11980–11983.
[23] A. Galembeck, O.L. Alves, J. Mater. Sci. 37 (10) (2002) 1923–1927.
[24] M. Gotic, S. Music, M. Ivanda, M. Soufek, S. Popovic, J. Mol. Struct. 744–747 (2005) 535–540.
[25] R. Strobel, H.J. Metz, S.E. Pratsinis, Chem. Mater. 20 (20) (2008) 6346–6351.
[26] R. Strobel, A. Baiker, S.E. Pratsinis, Adv. Powder Technol. 17 (5) (2006) 457–480.
[27] R. Strobel, S.E. Pratsinis, J. Mater. Chem. 17 (45) (2007) 4743–4756.
[28] K.A. Michalow, D. Logvinovich, A. Weidenkaff, M. Amberg, G. Fortunato, A. Heel, T. Graule, M. Rekas, Catal. Today 144 (1–2) (2009) 7–12.
[29] K.K. Akurati, A. Vital, J.-P. Dellemann, K. Michalow, T. Graule, D. Ferri, A. Baiker, Appl. Catal. B 79 (1) (2008) 53–62.
[30] AEROXIDE and AEROPERL titanium dioxide as photocatalyst, Tech. Rep. 1243, Degussa, p. 4, 2005.
[31] V. Petricek, M. Dusek, L. Palatinus, The Crystallographic Computing System, Institute of Physics, Praha, Czech Republic, 2006.
[32] R. Bacsa, J. Kiwi, T. Ohno, P. Albers, V. Nadtochenko, J. Phys. Chem. B 109 (12) (2005) 5994–6003.
[33] http://www.lighting.philips.com.
[34] A. Vital, A. Angermann, R. Dittmann, T. Graule, J. Topfer, Acta Mater. 55 (6) (2007) 1955–1964.
[35] K. Akurati, A. Vital, F. Reifler, A. Ritter, T. Graule, Technical Proceedings of the 2007 Nanotechnology Conference and Trade Show, Vol. 4, 2007, pp. 173–176.
[36] A. Ghosh, B.K. Chaudhuri, J. Mater. Sci. 22 (7) (1987) 2369–2376.
[37] R. Iordanova, E. Lefterova, I. Uzunov, Y. Dimitriev, D. Klissurski, J. Therm. Anal. Calorim. 70 (2) (2002) 393–404.
[38] Y.N. Blinovskov, A.A. Fotiev, Russ. J. Inorg. Chem. 32 (1) (1987) 145–146.
[39] J.D. Bierlein, A.W. Sleight, Solid State Commun. 16 (1) (1975) 69–70.
[40] J.A. Moulijn, A.E. Van Diepen, F. Kapteijn, Appl. Catal. A 212 (1–2) (2001) 3–16.
[41] R. Merkle, J. Maier, Z. Anorg. Allg. Chem. 631 (6–7) (2005) 1163–1166.
[42] R. Enriquez, B. Beaugiraud, P. Pichat, Water Sci. Technol. 49 (4) (2004) 147–152.
[43] Fachinformationszentrum Karlsruhe, Germany, Inorganic Crystal Structure Database, 2008.
[44] A.W. Sleight, H.Y. Chen, A. Ferretti, D.E. Cox, Mater. Res. Bull. 14 (12) (1979) 1571–1581.
[45] M. Stoltzfus, P. Woodward, R. Seshadri, J.-H. Klepeis, B. Bursten, Inorg. Chem. 46 (10) (2007) 3839–3850.
[46] M. Hirasawa, T. Orii, T. Seto, Appl. Phys. Lett. 88 (9) (2006) 093119.
[47] M. Winterer, Nanocrystalline Ceramics: Synthesis and Structure, no. 53 in Springer Series in Material Science, Springer, Berlin, 2002.
[48] T. Zhang, T. Oyama, A. Aoshima, H. Hidaka, J. Zhao, N. Serpone, J. Photochem. Photobiol. A 140 (2) (2001) 163–172.
[49] G. Liu, X. Li, J. Zhao, H. Hidaka, N. Serpone, Environ. Sci. Technol. 34 (18) (2000) 3982–3990.
[50] N. Serpone, D. Lawless, R. Khairutdinov, J. Phys. Chem. 99 (45) (1995) 16646–16654.
[51] S. Sakthivel, M. Janczarek, H. Kisch, J. Phys. Chem. B 108 (50) (2004) 19384–19387.
[52] G. Pacchioni, ChemPhysChem 4 (10) (2003) 1041–1047.
[53] J. Gautron, P. Lemasson, J.-F. Marucco, Faraday Discuss. Chem. Soc. 70 (1980) 81–91.
[54] T. Ihara, M. Miyoshi, M. Ando, S. Sugihara, Y. Iriyama, J. Mater. Sci. 36 (17) (2001) 4201–4207.
[55] A. Mills, J. Wang, J. Photochem. Photobiol. A 127 (1–3) (1999) 123–134.
[56] W. Spencer, J.R. Sutter, J. Phys. Chem. 83 (12) (1979) 1573–1576.
[57] M.J. O'Neil (Ed.), The Merck Index, 13th edition, Merck & Co., Whitehouse Station, 2001.
[58] T. Mohammad, H. Morrison, Photochem. Photobiol. 71 (4) (2000) 369–381.
[59] A. Houas, H. Lachheb, M. Ksibi, E. Elaloui, C. Guillard, J.-M. Herrmann, Appl. Catal. B 31 (2) (2001) 145–157.
[60] S. Kim, W. Choi, J. Phys. Chem. B 109 (11) (2005) 5143–5149.
[61] T. Rajh, J.M. Nedeljkovic, L.X. Chen, O. Poluektov, M.C. Thurnauer, J. Phys. Chem. B 103 (18) (1999) 3515–3519.
[62] X. Li, C. Chen, J. Zhao, Langmuir 17 (13) (2001) 4118–4122.
[63] J. Zhao, T. Wu, K. Wu, K. Oikawa, H. Hidaka, N. Serpone, Environ. Sci. Technol. 32 (16) (1998) 2394–2400.
[64] V.S. Ferreira-Leitao, J.G. da Silva, E.P.S. Bon, Appl. Catal. B 42 (2) (2003) 213–221.
[65] D. Gumy, S.A. Giraldo, J. Rengifo, C. Pulgarin, Appl. Catal. B 78 (1–2) (2008) 19–29.
[66] T.L. Thompson, J.T. Yates Jr., Top. Catal. 35 (3–4) (2005) 197–210.